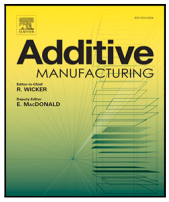
Additive Manufacturing 84 (2024) 104095



Contents lists available at ScienceDirect

Additive Manufacturing

journal homepage: www.elsevier.com/locate/addma



Research paper



# MeltpoolGAN: Melt pool prediction from path-level thermal history

Hongrui Chen [a], Xin Liu [a], Xingchen Liu [a,*], Paul Witherell [b]

[a] Intact Solutions, Inc., United States of America
[b] National Institute of Standards and Technology, United States of America

ARTICLE INFO

*Keywords:*
Laser powder bed fusion
Melt pool modeling
Generative machine learning

ABSTRACT

In metal laser powder bed fusion, a laser beam rapidly scans through a thin layer of powder. The laser heats up and liquefies the powder forming a melt pool. The melt pool characteristics affect the material property and physical performance of the part. Physical simulations of melt pool dynamics are computationally expensive and are often limited to a short laser scan. Alternatively, Finite Element (FE) simulations for part-scale thermal history are less computationally intensive but do not capture the detailed melt pool temperature profile and geometry in general. Accurate modeling of the high spatial and temporal thermal gradients inside and near the melt pool is essential to many applications of the thermal history including design and optimization of the laser scan path, material microstructure characterization, and deformation prediction.

In this work, we developed MeltpoolGAN, the first conditional Generative Adversarial Network (cGAN) to predict the melt pool image based on the simulated thermal history along the laser scan path. The integration of generative deep learning and thermal history simulation achieves melt pool-level accuracy while significantly reducing the physical and computational complexity. The data pair of thermal history and melt pool images for neural network training and validation are obtained through Contact-Aware Path Level (CAPL) thermal simulation and a co-axial melt pool monitoring system developed by NIST, respectively. The predicted melt pool morphology is validated against experimentally acquired melt pool images through geometric characteristics, including the length and width, of the melt pool.

## 1. Introduction

Laser powder bed fusion (LPBF) is an additive manufacturing technology that uses a laser beam controlled by a calculated toolpath to scan and melt thin layers of metal powders [1–3]. Near the center of the laser beam, the powder is rapidly heated to transform from solid powder to a liquid pool often referred to as the melt pool. When executing a scan strategy, not only the current scan path is heated but also the adjacent raw and solidified powder will be subjected to the heat transfer from the melt pool. Such rapid heating, cooling, and phase change leads to complex thermal history, which affects not only the solidified material microstructure [4] and properties [5,6] but also the geometry accuracy of the fabricated components [7]. Therefore the accurate modeling of detailed thermal history throughout the manufacturing process is critical to improving the mechanical performance and the quality of the part.

The most common approach to thermal history modeling is the finite element method (FEM) [8–10]. Like other numerical methods, FEM-based approaches require a significant amount of computational resources because they need small time steps to accurately model the high cooling rate [4] and high spatial resolution to represent small melt pools relative to the size of the part. The need for high resolution, small time steps, and the resulting high computational costs make it challenging to apply FEM-based approaches widely in practical engineering applications [11,12].

A Contact-aware path-level (CAPL) discretization approach was recently developed for simulating the path-level thermal history of the laser powder bed fusion process [13]. The CAPL approach was developed to improve the state-of-the-art in two aspects: (1) A discretization based on the manufacturing tool path, and (2) a localized thermal history computation based on the contact graph that results in higher computational efficiency. CAPL has been shown to outperform adaptive remeshing methods [14] in FEM simulation where the remeshing step is very expensive [15]. However, CAPL, similar to other part-scale thermal history simulations, neither employs a physics model that captures the complex fluid dynamics inside the melt pool nor carries high enough resolution to fully capture the extremely high spatial and temporal thermal gradients around the melt pool [16].

* Corresponding author.
*E-mail addresses:* hongrui@intact-solutions.com (H. Chen), xin@intact-solutions.com (X. Liu), xliu@intact-solutions.com (X. Liu), paul.witherell@nist.gov (P. Witherell).

https://doi.org/10.1016/j.addma.2024.104095
Received 1 November 2023; Received in revised form 16 March 2024; Accepted 18 March 2024
Available online 20 March 2024
2214-8604/© 2024 Elsevier B.V. All rights reserved.

Different from part-scale simulation, melt pool modeling generally involves simulating the behavior of molten metal during additive manufacturing processes, including the effects of heat transfer, surface tension, and fluid flow [17,18]. Computational fluid dynamics (CFD) is commonly involved in modeling melt pool behavior, which can be challenging due to the complex, turbulent flow that occurs during the process. Melt pool modeling is important to the understanding and improvement of metal AM processes as it provides detailed information in and around the melt pool that is not generally available through part-scale simulation. Due to extremely high spatial and temporal thermal gradients, the expensive computation often limits the melt pool simulation to a short laser scan [11,12].

In this work, we developed a novel hybrid approach to additive manufacturing thermal history simulation that combines the global, low-frequency, part-scale path-level thermal history field acquired through conventional physics-based simulation with local, high-frequency, melt pool images generated through machine learning. MeltpoolGAN is proposed to predict the melt pool images based on the path-level thermal history. Once trained, MeltpoolGAN can accurately and efficiently predict the melt pool image in any place along the scan path in near real-time. While offline simulations could support applications such as evaluating and optimizing for future builds, real-time and near real-time simulations enable a dynamic feedback loop and in situ corrective actions based on observed performance.

Specifically, we snapshot the path-level thermal history into a series of thermal distribution images that match the field-of-view and time steps of the captured melt pool images to work as the conditional inputs into the MeltpoolGAN. The data pair of thermal history and melt pool images for neural network training and validation are obtained through Contact-Aware Path Level (CAPL) thermal simulation [13] and a co-axial melt pool monitoring system on Additive Manufacturing Metrology Testbed (AMMT) developed by NIST, respectively. AMMT is a fully custom, open-platform laser powder bed fusion system built by the National Institute of Standards and Technology (NIST) [19,20]. This platform uses a coaxial melt pool monitoring (MPM) camera, which is capable of taking high-speed high-resolution melt pool frames [21]. The melt pool images are collected from experiments conducted on a custom-controlled laser powder bed fusion (LPBF) testbed on a nickel-alloy (IN625) solid surface [22]. While our approach is compatible with any physics-based thermal history simulation, here we model the part-scale thermal history with CAPL since it has been validated with the AMMT melt pool images and provides a fast, toolpath-based thermal history simulation. An overview of our approach is shown in Fig. 1.

The rest of the paper is organized as follows. In Section 2, we review related works in thermal history simulation, melt pool prediction, and Generative Adversarial Networks (GANs) for image synthesis. In Section 3, we propose MeltpoolGAN which predicts the melt pool image based on the computed part-scale path-level thermal history. We discuss the architecture of the neural network as well as the procedures and parameters used for training the model. In particular, we augment the CAPL thermal history by incorporating laser power and print path elapsed time into the input data. The two sources of input data to the neural network: the experimental acquisition of melt pool images and the part-scale thermal history simulation with CAPL, are briefly discussed in Section 3.2 and Appendix, respectively. In Section 4, we validate the proposed MeltpoolGAN by comparing the predicted melt pool image with the experimentally acquired ground truth images. The melt pool shape metrics, including length, width, and angle, are used to quantitatively evaluate the performance of the MeltpoolGAN. We observed improved melt pool prediction accuracy with data augmentation. We also discuss the limitations and challenges of the proposed methodology and provide insights into potential future work. In Section 5, we conclude the paper with remarks.

## 2. Related works

### 2.1. Thermal history and melt pool simulation

Generally speaking, thermal history modeling of the metal AM process can be categorized into melt pool modeling and part-scale thermal history modeling, depending on the scope of the simulation. The melt pool modeling requires high-fidelity modeling of multiphysics including powder dynamics, fluid dynamics of molten metal, and the interaction between molten metals and metal powders [23]. The melt pool modeling, therefore, is computationally expensive and often limited to a very short printing path [11,12]. For example, the simulation of a single-tracked melt pool takes up to 4000 min (60 h) for 390×210×50 $\mu m^3$ domain [18].

The finite element method (FEM) is a common approach [8–10] to simulate the path level LPBF process. Compared to melt pool simulation, FEM-based approaches simplify the complex multiphysics problem inside the melt pool. However, FEM approaches still can be computationally expensive for part-scale simulations, because it not only requires small time steps to capture the high cooling rate [4] but also requires a high spatial resolution to capture small melt pools compared to the part size. For example, a 2 mm × 2 mm 3-layer structure may require up to 10 h to simulate [10]. The need for high discretization resolution, small timesteps, and the associated high computational costs prohibits the broader adoption of FEM-based approaches in practical engineering applications [11,12].

Inherent strain [24] and flash heating [25,26], have been proposed to address the computational complexity in the part-level thermal history simulation, where homogeneity of thermal history within a single layer or even the entire part is, sometimes erroneously, assumed. Such a loss of path-level information often deteriorates the simulation accuracy [12] as material properties inside an additively manufactured part are heterogeneous and the overall performance of the part is highly sensitive to its manufacturing path [27]. Graph theory [28] is introduced to make a more efficient simulation of the LPBF process. Adaptive mesh [29] is also introduced to alleviate the computational cost. The effect of scanning strategies in the LPBF process is investigated in papers [30–32], where post-process measurements such as stresses are used to validate their approaches.

The CAPL approach was proposed for thermal simulation of the additive manufacturing process driven by a moving heat source, including fused deposition modeling (FDM) [33] and powder bed fusion (PBF) [13]. CAPL consists of a pre-processing stage and an execution stage. In the pre-processing stage, elements are generated by path-level discretization, and the contact-graph data structure is initialized. In the execution stage, simulation based on the lumped-capacitance heat transfer model assisted by the contact graph and elements. The active body algorithm is used to achieve linear time complexity. The element width and contact graph are updated by the element growth algorithm. Among the approaches simulating laser scanning on paths, CAPL is comparatively more efficient than the high-fidelity modeling and the FEM approach. For example, CAPL takes only 1 s to simulate a 0.39 mm (390 μm) scan where the aforementioned melt pool modeling approach took more than 60 h. A 2 mm × 2 mm 3-layer structure may require FEM-based approaches up to 10 h to simulate while CAPL simulates the same scanning path in 10 min. This is because CAPL has linear complexity regarding the scanning path length. In Section 4, we discuss the application of using an even lower-resolution discretization for CAPL to increase the simulation efficiency while retaining the meltpool prediction accuracy through MeltpoolGAN. As a lumped parameter model, CAPL could not model the shape of the melt pool effectively. However, this drawback will be mitigated with the proposed MeltpoolGAN in the rest of the paper.

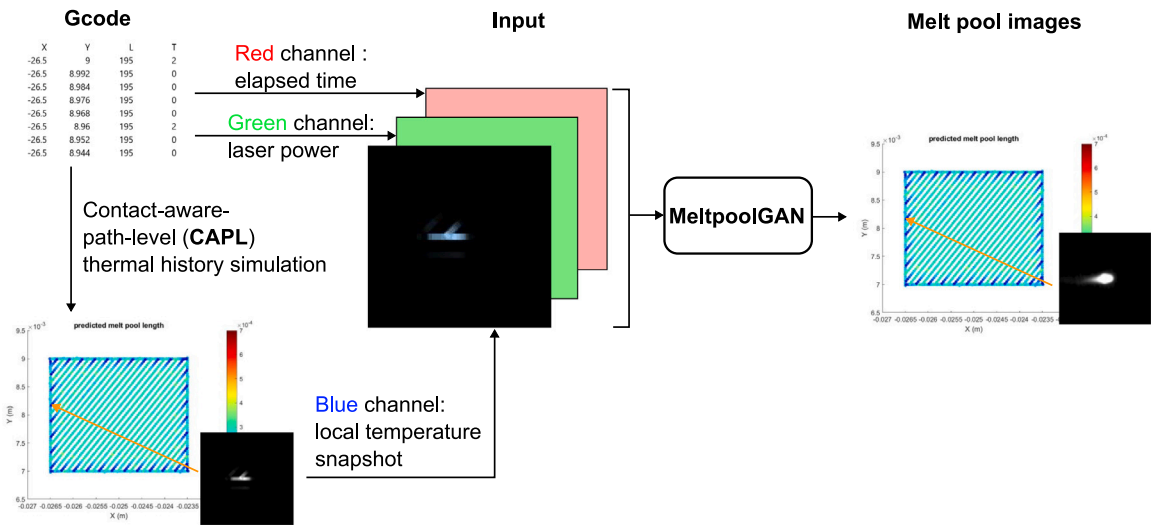



**Fig. 1.** Flowchart of MeltpoolGAN. AMMT monitors the meltpool shape and we also record the corresponding AM process parameters. The AM process parameters is then sent to CAPL to simulate thermal history. We augment the thermal history with laser power and path angle obtained from the process parameters. The augmented thermal history image serves as the input/condition to our GAN. The ground truth is obtained from AMMT directly. The MeltpoolGAN is then trained to predict meltpool based on CAPL thermal history.

### *2.2. In-situ monitoring of thermal history and melt pool*

There have been several ways temperature and melt pool behaviors have been observed or correlated, including thermocouples, photodiodes, pyrometers, and thermal cameras, to list a few [34]. Thermocouples are small devices that directly measure temperature at specific locations, which can provide accurate temperature data with high temporal resolution [35,36]. On the other hand, thermal cameras are imaging devices that use infrared radiation to capture a heatmap of the temperature distribution across the workpiece [37]. High-speed cameras have also been used in detecting the splatter pattern of the melt pool [38,39].

Thermal cameras have been integrated into the laser optical path as co-axial imaging [40] or stationed outside the optical path as off-axis imaging [41]. Co-axial measurements have a better spatial resolution around the melt pool and provide more accurate temperature information near the laser beam [42]. In contrast, off-axis measurements provide a more global view of the temperature distribution across the entire workpiece. Machine learning methods have been applied to melt pool identification and categorization [43]. In Section 3, we will discuss the NIST AMMT dataset in more detail.

Machine learning techniques have been applied to LPBF process monitoring. Recent work by Liu et al. used Pix2Pix and ResNet34 to predict melt pool geometries with acoustic and photodiode input [44]. Other machine learning application includes defect detection [45–47], quality monitoring [48–50], melt pool geometry and characteristic modeling [51,52].

### *2.3. Generative adversarial networks*

Recent progress in machine learning-enabled an exponential increase in research into computer vision and image processing. Among such progress is Generative Adversarial Networks (GAN) [53]. First proposed by Goodfellow, GAN consists of two competing neural networks namely the generator and the discriminator. The purpose of the generator is to generate images based on a given input, while the discriminator judges the quality of the generated images. During the training of GAN, the two neural networks evolve together as the generator tries to generate images that the discriminator cannot discern as "real" or "fake" and the discriminator tries to catch the generator's "fake" image. With the invention of GAN, much research that followed improved the capability of GAN. One such improvement is Pix2Pix [54]. In contrast to the original GAN that relies on random noise or a vector as inputs for the generator, Pix2Pix's generator takes in a two-dimensional image. Through the use of neural networks, GAN enables a variety of tasks that originally took a longer time to perform, such as transforming satellite imagery into maps or hand sketches into photos. A recent example used the cGAN's input of a coarse scale density field for microstructure reconstruction [55].

## 3. MeltpoolGAN

### *3.1. Melt pool image prediction from CAPL thermal history*

We construct our network based on the architecture of Pix2Pix [54]. There are several key advantages to this approach compared to other variations of conditional GANs (cGAN). Compared to other cGAN architectures using one-dimensional latent vectors, the image-based condition establishes a direct spatial correspondence between the input and outputs. This not only facilitates the direct visual inspection of the generated results but also enables more complex relationships between input and the target image to be learned without any additional pre and/or post-processing. Similar to other GANs, the architecture of the neural network consists of a generator and a discriminator. The generator consists of convolution layers stacked together followed by deconvolution layers. In addition, the convolution and deconvolution layers are connected with skip connectors. The discriminator consists of convolution layers to downsample the generated image from the original resolution to a lower resolution. Interested readers may refer to the paper [54] for an in-depth discussion about network architecture.

The main input to the cGAN consists of snapshots of normalized CAPL thermal history, such that 0 corresponds to 293K and 1 corresponds to 1563K. We rasterized the path with 120 × 120 pixel images that have the same field of view as the AMMT dataset. A nominal 4-pixel width is used to represent the width of the path. As mentioned in Section 1, MeltpoolGAN is compatible with any physics-based thermal history simulation. In this paper, we model the thermal history with CAPL since it has been validated with the AMMT melt pool images and provides a fast toolpath-based thermal history.

In the pre-processing stage, we add additional fictitious paths to the path-level discretization algorithm such that the entire domain is filled with real paths and fictitious paths. The contacts between all elements are initialized according to the contact graph. We initialize all elements with solid material properties since a solid surface is used

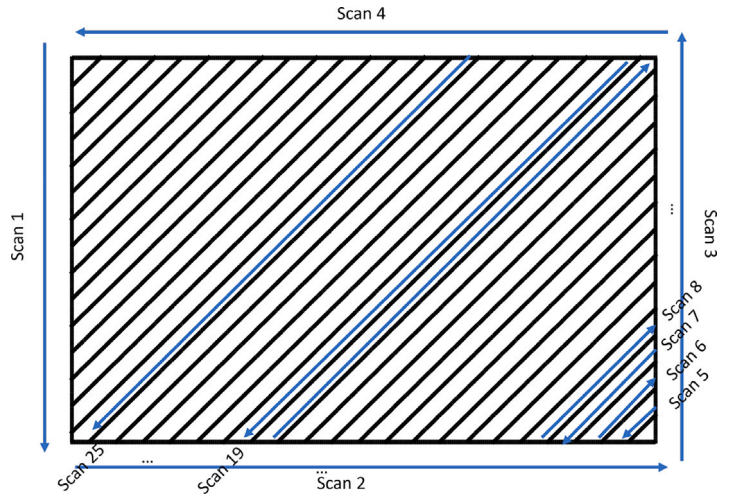



**Fig. 2.** Numbering of scan vectors. The scan pattern for the NIST AMMT dataset consists of an outer shell path (Scan 1–4) and a hatching pattern (Scan 5+) for the infill. From Scan 19–25, the total scan distance is equal and the longest for all of the hatching infill patterns. We only show the scan pattern where the laser is turned on in this figure.

in the present paper. Table 1 shows the relevant process parameters and material properties of IN625. We then snapshot the thermal history into a series of thermal distribution images that match the field-of-view and time steps of the captured melt pool images by AMMT. The resolution is 120 by 120 pixels. Since MeltpoolGAN is trained on a 256 by 256 image input, we scale the image accordingly. We further augment the input with uniform melt pool orientations, normalized laser power, and the elapsed time since the start of each toolpath segment.

**Uniform melt pool orientations** Rotations are applied to both the CAPL thermal history images and the AMMT melt pool images such that all melt pool orientations are the same. Specifically, We use the scipy.ndimage.rotate with 3rd order spline interpolation for both simulation and experiment data. By simply re-orienting, we do make assumptions — namely that the melt pool shape is maintained based on directional vectors. This not only reduces the complexity of the space that MeltpoolGAN needs to capture but also increases the number of effective training data. The orientation of each melt pool image can be calculated directly from toolpath information.

**Normalized laser power** The laser power density has been shown to have a direct impact on the melt pool morphology. Even though the effect of the laser power is already captured in the CAPL part-scale thermal history simulation as part of its input, we introduce the laser power as an input to allow the MeltpoolGAN to establish an explicit link to melt pool morphology. The scan strategy adopted for our experimental data is to vary the laser power to maintain a constant melt pool size [22] (see next section for details). As a result, we include the laser power as an additional input to the MeltpoolGAN to examine its effects on melt pool prediction. We normalize the power between 0–195 W or 180–195 W and added in the green channel of the input image. We note that this normalization here is based on the specific dataset, others may run at a higher wattage. The effect of laser power and its normalization on melt pool prediction will be discussed in the next section.

**Elapsed time since laser start** The motivation to add elapsed time is to capture the dynamic behavior during the start of each scan path. The laser absorptivity varies even during constant laser power and constant speed solidification as it depends on a variety of melt pool characteristics and surface conditions. Understanding absorptivity and surface conditions itself is an important topic where many studies have been conducted [56,57]. In the CAPL simulation of thermal history, a constant laser absorptivity is used for simplicity. However, such constant laser absorptivity does not capture the dynamic evolution of the melt pool at the beginning of each scan path. For example, in Fig. 3, we can observe distinctive spikes in the length and width. These spikes correspond to the start at each scan path. As a result, we propose to augment the input data with a temporal element to the MeltpoolGAN by adding the elapsed time of each toolpath. Specifically, the elapsed time is calculated from the beginning of each scan path. Since AMMT captures the melt pool images at constant intervals, the elapsed time can be calculated based on the increment of the melt pool images. The longest possible elapsed time occurs in Line 25 of the path and we use the time of Line 25 to normalize the elapsed time. Again we should note that these are modifications made for the specific dataset. The elapsed time is then encoded into one of the color channels in the CAPL thermal history snapshot.

The conditional GAN's objective can be expressed as

$$\mathcal{L}_{\text{GAN}}(G, D) = \mathbb{E}_y[\log D(y)] + \mathbb{E}_{x,z}[\log(1 - D(x, G(x, z)))] \tag{1}$$

where generator G tries to minimize the objective against a discriminator D. Pix2Pix also includes the L1 loss between the generated image and ground truth.

$$\lambda\mathcal{L}_{L1}(G) = \mathbb{E}_{x,y,z}[\|y - G(x, z)\|] \tag{2}$$

The combined objective function is

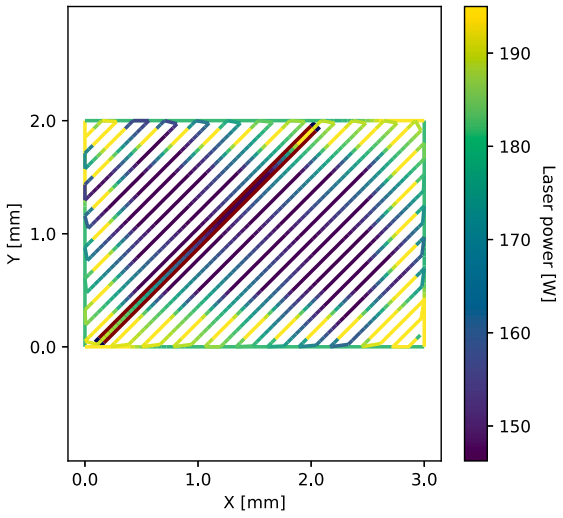
$$G^* = arg\min_G \max_D \mathcal{L}_{cGAN}(G, D) + \lambda\mathcal{L}_{L1}(G) \tag{3}$$

Where $\lambda = 100$ which encourages less blurring as reported in [58]

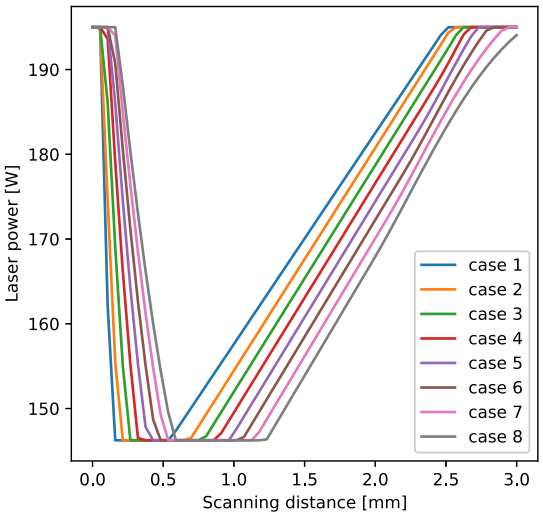
Similar to Pix2Pix [58], MeltpoolGAN is trained with 40,000 steps. For the training dataset, we randomly selected 100 images from each of the cases. This sums to 800 total images across 8 cases to be used to train MeltpoolGAN. We use a single image for every batch, the total epoch is 50. The same architecture and hyperparameters from Pix2Pix are used for training MeltpoolGAN. The TensorFlow implementation of Pix2Pix can be found at [59]. The model is trained on an RTX 3080 GPU and the training time is 30 min. The training history plot for GAN loss, discriminator loss, and, L1 loss is shown in Fig. 5. Each melt pool image generation takes 0.06 s.

### 3.2. NIST AMMT melt pool image dataset

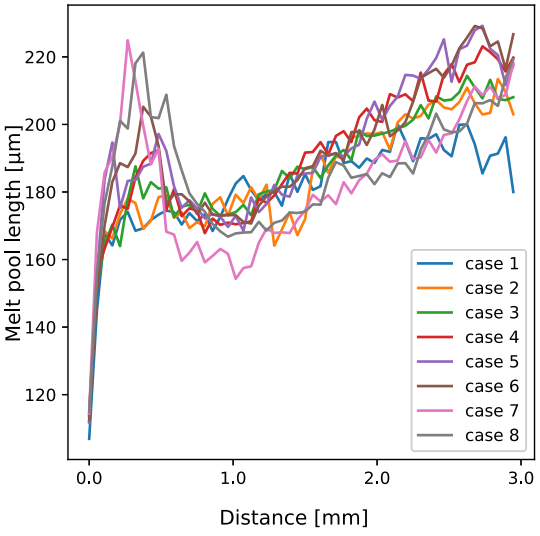
The experiment dataset used in the present paper is the melt pool frames acquired on the Additive Manufacturing Metrology Testbed built by NIST. The resolution of each frame is approximately 7.13 um/pixel. An example of the melt pool frame is shown in Fig. 4. As discussed in the previous sections, the digital value on the frames corresponds to the temperature which can be determined by the Sakuma–Hattori Equation. A threshold of the digital value corresponding to the melting temperature is needed to extract the melt pool shape. Based on



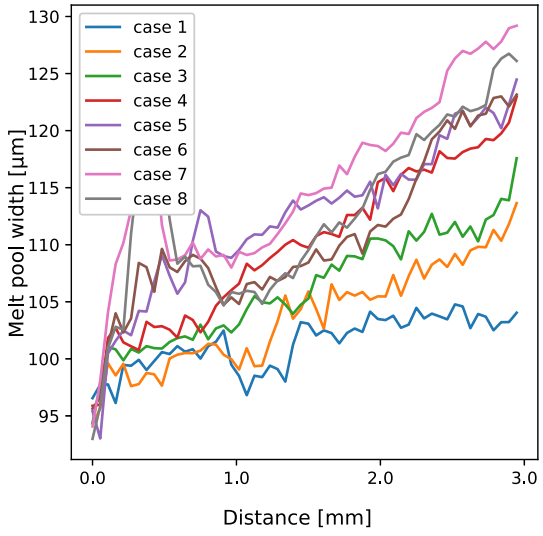

(a) Laser power plotted along the toolpath for case 8. The specific scan path (scan 25) for (b,c,d) is highlighted in red




(b) Laser power for 8 cases along scan 25




(c) Melt pool length evaluated along scan 25




(d) Melt pool width evaluated along scan 25

**Fig. 3.** Dataset analysis for the laser power and melt pool length and width properties from AMMT.



**Fig. 4.** An example of meltpool frame (left) acquired on the Additive Manufacturing Metrology Testbed by NIST and the binarized result (threshold is 80 out of 255).

other experiments conducted on AMMT, we use 80 out of 255 as the threshold.

We use the 8 cases from the dataset with varying laser power and every case consists of 1498 melt pool images at various locations during the laser scan. The scanning paths are shown in Fig. 2 and all 8 cases use the same scanning path. The laser power ranges between 180 to 195 [W]. In all 8 cases, the laser power was lowered to decrease the variance in melt pool size based on the residual heat factor in an earlier NIST study. Interested readers may refer [22] for details. For every case, the 1498 melt pool images come from sampling on a single-layer scanning on an Inconel 625 solid surface. The images come from an even sampling at the frequency of 20 kHz when the laser is turned on.

All melt pool lengths from the experimental melt pool image data are plotted as line graphs shown in Fig. 3. The vertical axis represents the melt pool length, and the horizontal axis represents the frame number. Since the scanning path is geometrically the same for all cases and the frames are sampled at the same time sequence, the same frame number results in the same relative location in every case.

In all cases, the melt pool lengths periodically drop to zero. This is due to a synchronization issue of the melt pool monitoring system such that the first image at the beginning of each scan is captured before the laser starts. In addition, excessively long melt pools are observed near the beginning of some scan vectors. Upon closer examination, this

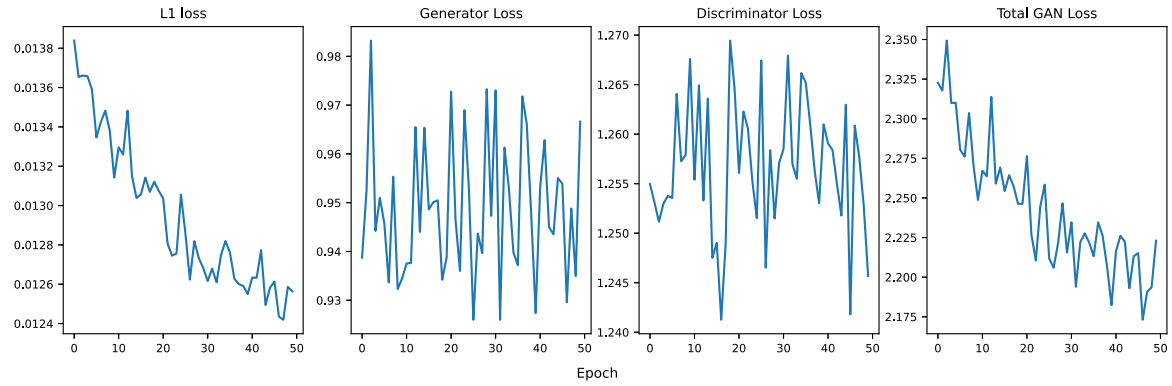



**Fig. 5.** Convergence history during training. A total of 40,000 training steps are used. We averaged the loss for every epoch. The loss is averaged for each epoch. We observed the L1 loss and total GAN loss decreased during the training. While generator and discriminator loss remains steady showing neither the generator nor the discriminator is dominating during the training, which means a successful training of GAN in general.

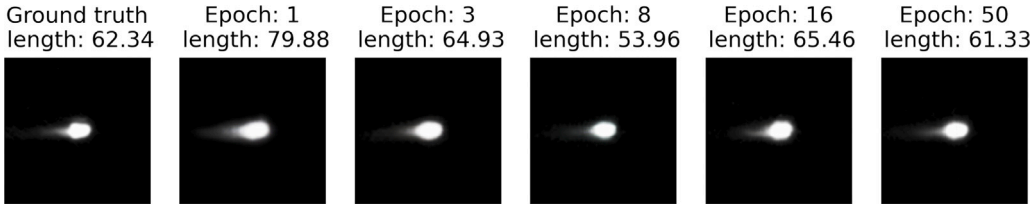



**Fig. 6.** Snapshot of the meltpool prediction during training with a sample image from the testing dataset. We observe that GAN gradually learns the correspondence between the thermal history and the melt pool shape. A total of 50 epochs is used during training. We evaluate the length of the melt pool at these epochs and observe the length error gradually reduces.

**Table 1**
Process parameters and material properties of IN625 [60].

| | |
|---|---|
| Solidus temperature $T_S$ | 1563 K |
| Liquidus temperature $T_L$ | 1623 K |
| Environmental temperature | 293 K |
| Latent heat of fusion | 290 kJ/kg |
| Specific heat ($T \leq T_S$) | 338.98 + 0.2437×T [J/kg K] |
| Specific heat ($T \leq T_L$) | 735 J/kg K |
| Thermal conductivity, ($T \leq T_S$) | 5.331 + 0.015 ×T [W/(m K)] |
| Thermal conductivity, ($T \leq T_S$) | 30.05 W/(m K) |
| Density | 8440 kg/m$^3$ |
| Environmental convection coefficient | 10 W/(m$^2$ K) |
| Substrate temperature | 293 K |
| Laser spot diameter | 85 um |

**Table 2**
Relative length error of melt pool length predicted by MeltpoolGAN vs CAPL.

| Case No. | 01 | 02 | 03 | 04 |
|---|---|---|---|---|
| CAPL Relative error (%) | 9.62 | 8.81 | 8.44 | 8.21 |
| GAN Relative error (%) | 5.5 | 5.1 | 4.7 | 4.9 |
| Low res CAPL relative error (%) | 24.0 | 23.6 | 23.3 | 22.9 |
| Low res CAPL GAN relative error (%) | 9.9 | 7.3 | 6.2 | 5.9 |
| Case No. | 05 | 06 | 07 | 08 |
| CAPL Relative error (%) | 8.87 | 9.03 | 11.66 | 12.70 |
| GAN Relative error (%) | 5.4 | 5.9 | 9.0 | 9.5 |
| Low res CAPL relative error (%) | 25.3 | 24.7 | 30.6 | 29.0 |
| Low res CAPL GAN relative error (%) | 7.2 | 7.0 | 10.9 | 9.9 |

is due to the gas plume being mischaracterized as the melt pool after thresholding (see Fig. 4). In both these cases, the extracted melt pool lengths do not correspond to the real melt pool length and, therefore, are excluded from the training and validation of meltpoolGAN (see Table 1).

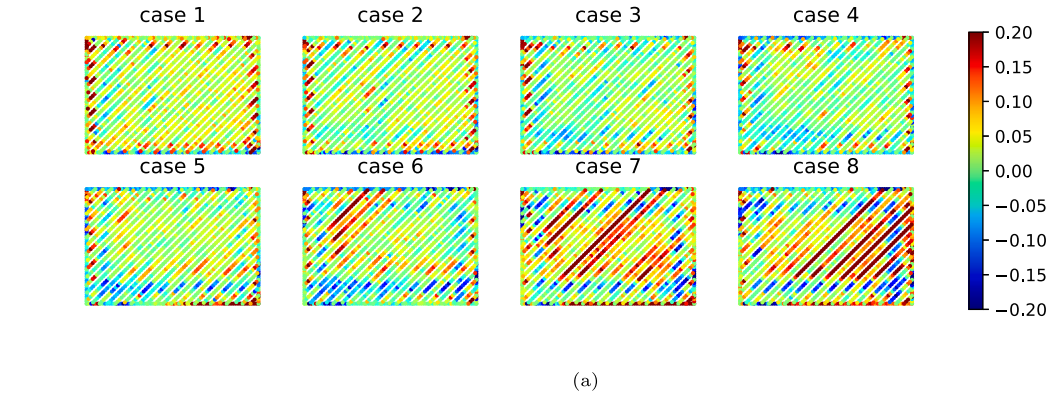
## 4. Validation of MeltpoolGAN through melt pool shapes

We validate the MeltpoolGAN's performance by comparing the length and width of the melt pool with AMMT experiment results. Meltpool images from AMMT and MeltpoolGAN are binarized to distinguish the melting and solid regions with the threshold (see Fig. 4). The melt pool shape is approximated by Scikit-image's regionprops function [61], which will approximate the melt pool shape by an ellipse that has the same normalized second central moments as the region. The melt pool length and width are computed as the length of the major and minor axis.

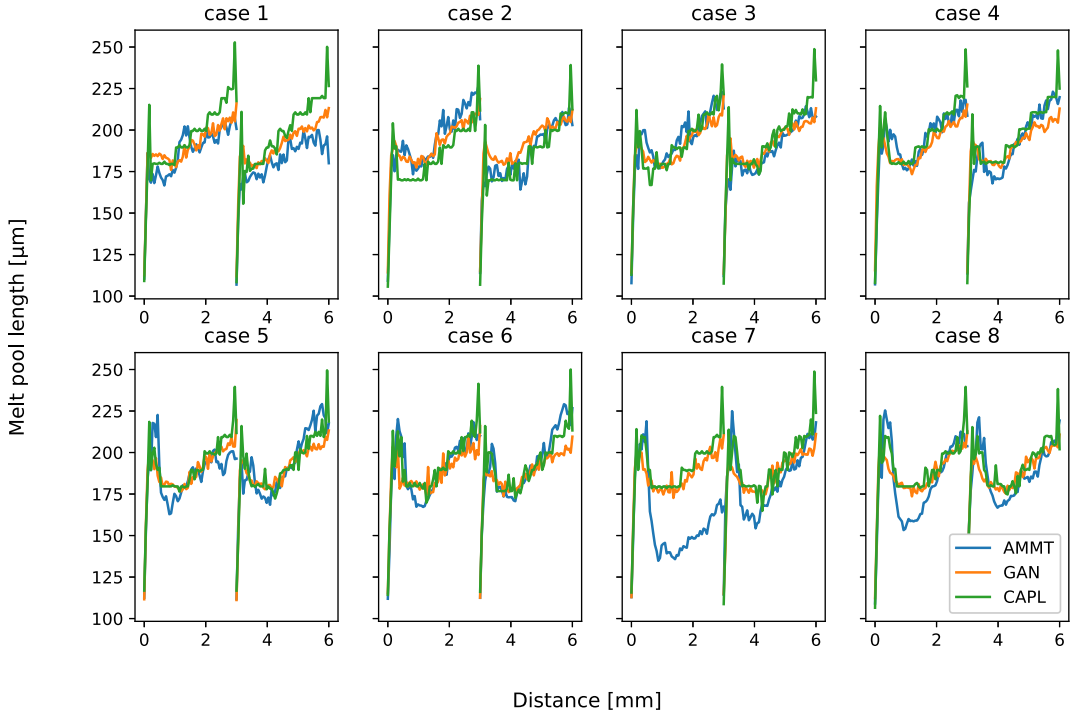
We use the length from AMMT melt pool as the ground truth and the relative errors for CAPL and MeltpoolGAN are calculated accordingly. We evaluated the melt pool length and width between AMMT and MeltpoolGAN for all 8 cases to calculate the error. The detailed comparisons for length and width on Scan 24 and 25 are plotted in Figs. 7 and 8, respectively. When looking at each individual path between the cases, we observe that the error is higher at the beginning of each scan. This could be caused by the high transient nature of the melt pool within the first couple of data collection points. When comparing the error case by case, we observe that the length error in case 8 and the width error in case 1 displayed path orientation dependency. Yet, neither CAPL nor MeltpoolGAN captured the change in melt pool geometry based on scan direction. This could be caused by slight inconsistency during data collection. We also show the melt pool prediction and length evaluation during training at selected epochs in Fig. 6. In addition, we plotted the first 10 melt pool samples along scan path 25 in Fig. 9 to compare the actual prediction of the MeltpoolGAN against AMMT ground truth images. We observe that MeltpoolGAN captures the temporal evolution of the melt pool morphology. The statistics of relative errors in melt pool length and with for all cases are summarized in Tables 2 and 3, respectively.

### 4.1. Effect of data augmentation

In this section, we conduct an ablation study to evaluate the effect of data augmentation by comparing the effect of time, rotation, and laser power. Six total numerical experiments were conducted with a




(a)




(b)

**Fig. 7.** (a) Scatter plot for the length error between AMMT ground truth and MeltpoolGAN. (b) Comparing the meltpool length at scan 24 and 25 for AMMT, MeltpoolGAN across all 8 datasets.

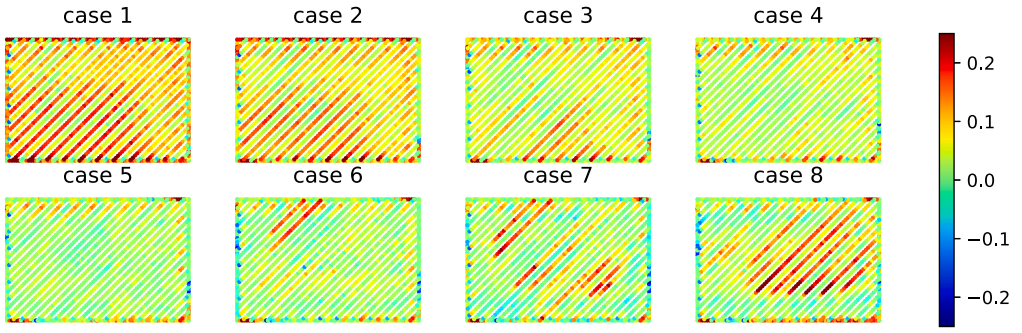
**Table 3**
Relative width error of melt pool width predicted by MeltpoolGAN.

| Case No. | 01 | 02 | 03 | 04 |
|---|---|---|---|---|
| GAN Relative error (%) | 11.4 | 9.2 | 6.5 | 5.3 |
| Low res CAPL GAN relative error (%) | 15.1 | 12.0 | 8.6 | 7.0 |
| Case No. | 05 | 06 | 07 | 08 |
| GAN Relative error (%) | 3.8 | 4.4 | 5.3 | 6.8 |
| Low res CAPL GAN relative error (%) | 5.6 | 5.6 | 5.7 | 7.6 |

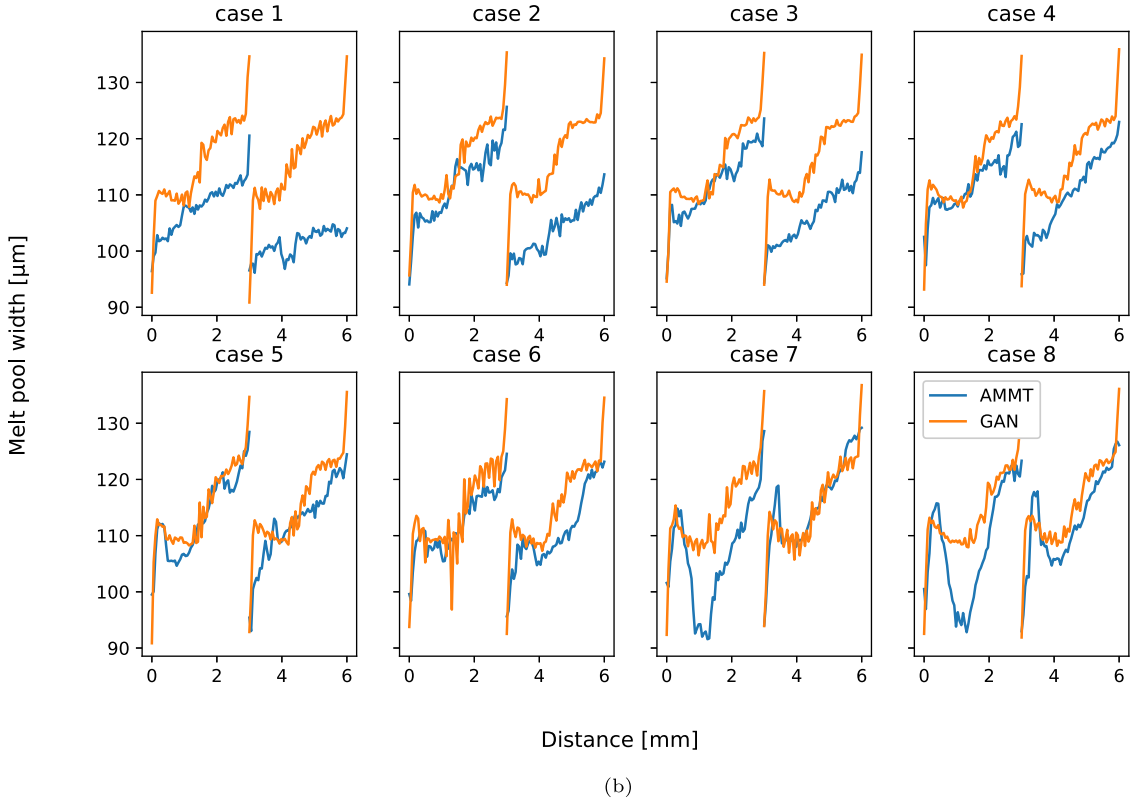
combination of time, rotation, and laser power enabled and disabled. The result is summarized in Table 4. We observe that compared to cGAN trained on the original dataset, adding rotation offered the most significant improvements in terms of error prediction in length. When only comparing the dataset with and without rotation while not adding time and laser power, we observe an average length error reduction of 49%. Adding rotation effectively increases the number of training samples and reduces the need for the GAN to learn to melt pool geometry in all eight print directions into a single direction. We also observe that adding time alone does not improve the network performance in which only the combined parameters of time, rotation, and laser power can further improve the result. When time, rotation, and power are added, we observe the best performance of the MeltpoolGAN in predicting melt pool length.

### 4.2. MeltpoolGAN's accuracy improvement

In this section, we compare the performance of the melt pool prediction between MeltpoolGAN and CAPL. We limited the comparison to length only as CAPL's toolpath-based discretization does not provide the melt pool width directly [13]. In Fig. 7, we observe that compared to CAPL, the length error is decreased in almost all regions in the domain. The improvements in MeltpoolGAN are especially noticeable




(a)




(b)

**Fig. 8.** (a) Scatter plot for the width error between AMMT ground truth and MeltpoolGAN. (b) Comparing the meltpool width at scan 24 and 25 for AMMT, MeltpoolGAN across all 8 datasets.

**Table 4**
Relative error of melt pool length predicted by MeltpoolGAN.

| Time | Rotation | Power | Avg length error | Avg width error |
|---|---|---|---|---|
| ✗ | ✗ | ✗ | 0.140 | 0.101 |
| ✓ | ✗ | ✗ | 0.144 | 0.364 |
| ✗ | ✓ | ✗ | 0.072 | 0.073 |
| ✓ | ✓ | ✗ | 0.080 | 0.113 |
| ✓ | ✗ | ✓ | 0.124 | 0.131 |
| ✓ | ✓ | ✓ | 0.063 | 0.073 |

at the beginning of each scan line. We also observed that the errors in MeltpoolGAN prediction generally correlate with the errors in CAPL prediction, albeit smaller in magnitude, indicating the effectiveness and importance of accurate conditional inputs. Furthermore, due to the melt pool's dependency on mesh size for CAPL simulation, we observe some stepping behavior with CAPL while MeltpoolGAN's is smoother.

### 4.3. Low-resolution CAPL result as inputs

CAPL simulates the thermal history along the toolpath where discretization will determine the element size used for simulation. Just like other numerical simulation approaches, CAPL also has numerical stability and convergence issues. For CAPL, the element size and timestep need to be small enough to capture the thermal history accurately. Generally speaking, firstly the element size and timestep need to be small enough to ensure numerical stability, then as the element size and timestep further decrease, the numerical solution will converge to the true solution.

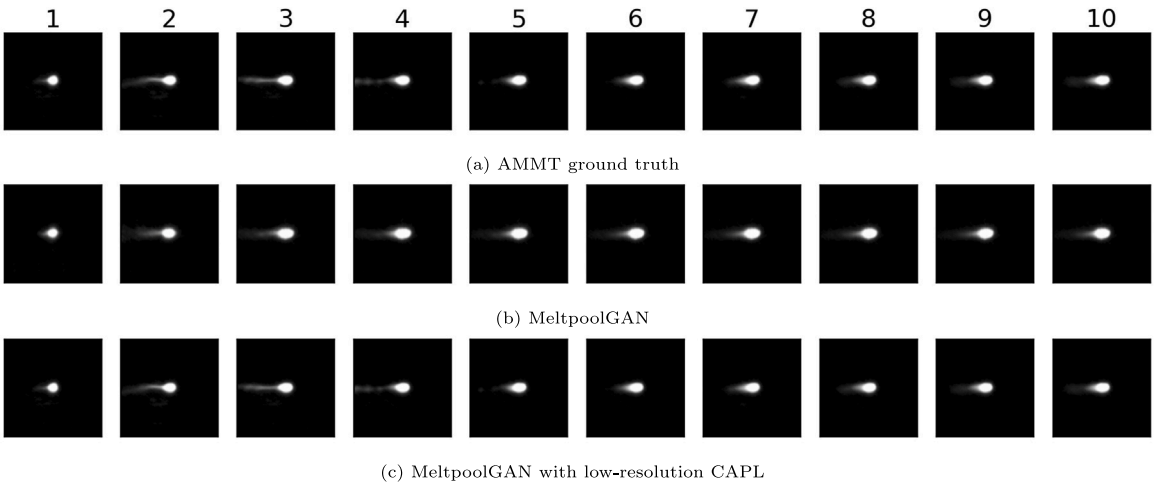



**Fig. 9.** MeltpoolGAN prediction (top) and AMMT ground truth(bottom) during the first 10 points on meltpool line 25. The dataset is case 04.

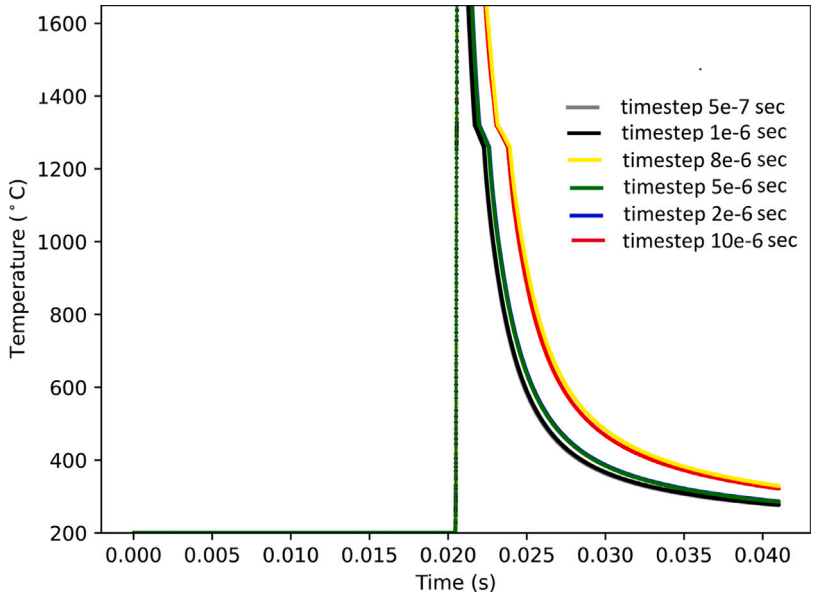



**Fig. 10.** CAPL thermal history when different timestep size is used. The timestep needs to be small enough to converge.

Larger timestep and element size are more advantageous when considering the simulation efficiency, however, timestep size and element size must be compatible to ensure numerical stability [62]. One can potentially use low-resolution, specifically, larger element sizes and larger timesteps, to achieve faster simulation, but the accuracy cannot be guaranteed. Though the trends are similar, the numerical values do not necessarily converge to the true solution. For example, we compare the simulation results of a single scan test (laser 195 W, 1 m/s) on an IN625 bare plate using different timestep sizes. As shown in Fig. 10, though the trends are similar for various timestep from $10^{-5}$ to $10^{-5}$ s, the thermal history needs the timestep to be small enough ($10^{-6}$ s) to converge.

MeltpoolGAN can use the low-resolution CAPL simulation results when the trend remains the same. We would like to experiment if training is possible with a lower resolution CAPL simulation. Specifically, we ran CAPL with a 10 times increase in element size which resulted in a reduction of the simulation time by 100 times for a single-layer scan. The decrease in simulation time could potentially reach 1000 times for a multilayer build. As a result, the increase in the element size also increased the error of CAPL simulation results. We then use the low-resolution simulation result from CAPL as the input to MeltpoolGAN. The melt pool length of low-resolution CAPL and GAN are summarized in Table 2. A snapshot of the first 10 melt pools and the ground truth AMMT image is also plotted in Fig. 9. We observe that MeltpoolGAN dramatically reduced the error while maintaining a consistent prediction of melt pool images, which allows us to further increase the computational efficiency in simulating the high resolution, high fidelity, melt pool-level thermal history at the part scale.

## 5. Conclusion

In conclusion, we developed MeltpoolGAN, a melt pool-level part-scale thermal history prediction system using cGAN with CAPL thermal history simulation and laser parameters data augmentation as inputs. We evaluated the effect of different augmentations, including laser power, the time elapsed for each toolpath, and rotation of the melt pool image, on the accuracy of MeltpoolGAN predictions. We validated the proposed approach through the geometric characteristics, including length, width, and angle, of the melt pool by comparing the MeltpoolGAN predictions against AMMT melt pool images. The results show that MeltpoolGAN significantly reduces prediction error compared to both CAPL and low-resolution CAPL predictions.

Simulation efficiency is an imperative issue to be addressed in the LPBF process. Real-time simulation of melt pool shape can be very useful in applications such as dynamic feedback loops or in situ corrective actions based on observed performance. The design of a process plan to optimize the thermal history and other thermally induced properties also requires fast simulation tools.

Currently, MeltpoolGAN only predicts the melt pool in 2D. This is partially due to the AMMT melt pool image data, which is limited to 2D. However, as real-time depth monitoring systems become available, we may include encoding depth information using the grayscale value in 2D for minimal changes to the neural network architecture. A more comprehensive encoding of depth information can be achieved using 3D convolution layers for the underlying cGAN. Moreover, the proposed MeltpoolGAN may serve as a basis for active melt pool control, where the speed and power of the laser can be varied to achieve a targeted melt pool morphology. Last but not least, the additive manufacturing community has shown that there is a degree of variability in the PBF process, where the meltpool width at the same time and location may be different despite the process parameters being identical. Even though such randomness has not caused notable difficulty in our training processes, direct application of the meltpool images without properly addressing the variability and randomness may cause difficulty in the application of the proposed approach in other datasets.

## CRediT authorship contribution statement

**Hongrui Chen:** Writing – review & editing, Writing – original draft, Methodology, Investigation, Data curation, Conceptualization. **Xin Liu:** Writing – review & editing, Visualization, Validation, Investigation, Data curation. **Xingchen Liu:** Writing – review & editing, Supervision, Project administration, Methodology, Conceptualization. **Paul Witherell:** Writing – review & editing, Funding acquisition.

## Declaration of competing interest

The authors declare that they have no known competing financial interests or personal relationships that could have appeared to influence the work reported in this paper.

## Data availability

Data will be made available on request.

## Acknowledgments

The authors thank Ho Yeung from the National Institute of Standards and Technology for providing the melt pool monitoring data and helpful discussions. This research was supported by the National Institute of Standards and Technology, United States. The responsibility for errors and omissions lies solely with the author. We thank the anonymous reviewers for their insightful comments and suggestions.

## Appendix. PBF-CAPL

In our previous work, we developed a path-level thermal simulation framework for the LPBF process called PBF-CAPL [13]. The PBF-CAPL is developed based on a Contact-aware path-level (CAPL) discretization approach was developed for simulating the path-level thermal history of a moving heat source [15,33,63]. CAPL tailors discretization to the manufacturing toolpath and adopts locality for linear time complexity in part-scale thermal history simulations. We validate the new approach against melt pool images captured with the co-axial melt pool monitoring (MPM) system on the Manufacturing Metrology Testbed (AMMT) developed at the National Institute of Standards and Technology (NIST) [22,64]. Excellent agreements in the length and width of melt pools are found between simulations and experiments conducted on a custom-controlled laser powder bed fusion (LPBF) testbed on a nickel-alloy (IN625) solid surface. A brief introduction is given below for PBF-CAPL. The readers might find more details in our previous paper [13].

There are two main stages in PBF-CAPL: the pre-processing stage and the execution stage. In the pre-processing stage, there is a path-level discretization algorithm that discretizes the simulation domain into scanning-path-associated elements. The elements are connected by a data structure called a contact graph. In the execution stage, a lumped-capacitance heat transfer model is used to simulate the moving-laser-driven convection–conduction–radiation problem. The linear complexity is achieved by utilizing a concept we call "active body": a region that is "close" to the current heat source either in time or space. Only elements in the active body are updated in each time step. The lazy update is applied for the region outside the active body.

In the preprocessing stage, the data structure is prepared for the execution stage. In the path-level discretization algorithm, the scan path and laser power information are extracted from the input file. Along with these real paths, fictitious paths are added to fill the entire domain if it is needed. The real and fictitious paths are discretized into elements. PBF-CAPL considers an element to be associated with a sub-path of the real or fictitious path. Each element is approximated as a path-aligned box defined by its length $L$ (equal to the length of the sub-path), width $W$, and height $H$ (equal to the layer height). The cross-sectional shape is a rectangle $W \times H$ which is perpendicular to the scanning direction. The top surface of the element is approximated by a rectangle $L \times H$. The width of an element $W$ is determined by a Voronoi diagram of the real and fictitious paths. For parallel scanning lines, $W$ will be simply the hatching space. The elements are connected by the contact graph. The contact graph is composed of vertices which represent elements and edges which represent the contacts between adjacent elements. A contact will be generated if two elements overlap.

In the execution stage, a lumped-capacitance heat transfer model is used to simulate the thermal process. The equation for an element $i$ is:

$$m_i c_i \dot{T}_i = Q_i + q_i \tag{4}$$

where $m_i$, $c_i$, $T_i$ are the mass, thermal capacity, and the temperature of element $i$, respectively. $Q_i$ and $q_i$ are the heat transfer on the boundary of element $i$ and the laser input energy on element $i$, respectively. $Q_i$ further includes the convection from the environment, radiation to the environment, and the conduction from other elements.

In each step, computation based on the lumped-capacitance model is conducted in the "active body". The active body is a region near the laser. The active body moves along with the laser. The size of the active body is determined based on trial and experience. A proper size of the active body ensures the cooling outside the active body the analytical Newton's cooling law is applicable. Utilizing the active body ensures the computation is only needed in the active body in each step. The thermal history outside the active body needs to be updated by Newton's cooling only when the elements go into the active body again.

## References

[1] S. Vock, B. Klöden, A. Kirchner, T. Weißgärber, B. Kieback, Powders for powder bed fusion: A review, Prog. Addit. Manuf. 4 (4) (2019) 383–397.
[2] V. Bhavar, P. Kattire, V. Patil, S. Khot, K. Gujar, R. Singh, A review on powder bed fusion technology of metal additive manufacturing, in: Additive Manufacturing Handbook, CRC Press, 2017, pp. 251–253.
[3] D.D. Singh, T. Mahender, A.R. Reddy, Powder bed fusion process: A brief review, Mater. Today: Proc. 46 (2021) 350–355.
[4] R. Acharya, J.A. Sharon, A. Staroselsky, Prediction of microstructure in laser powder bed fusion process, Acta Mater. 124 (2017) 360–371.
[5] A. Hilaire, E. Andrieu, X. Wu, High-temperature mechanical properties of alloy 718 produced by laser powder bed fusion with different processing parameters, Addit. Manuf. 26 (2019) 147–160.
[6] K. Inaekyan, A. Kreitcberg, S. Turenne, V. Brailovski, Microstructure and mechanical properties of laser powder bed-fused IN625 alloy, Mater. Sci. Eng. A 768 (2019) 138481.

[7] Z. Luo, Y. Zhao, A survey of finite element analysis of temperature and thermal stress fields in powder bed fusion additive manufacturing, Addit. Manuf. 21 (2018) 318–332.

[8] W. Yan, J. Smith, W. Ge, F. Lin, W.K. Liu, Multiscale modeling of electron beam and substrate interaction: A new heat source model, Comput. Mech. 56 (2) (2015) 265–276.

[9] A.J. Dunbar, E.R. Denlinger, M.F. Gouge, P. Michaleris, Experimental validation of finite element modeling for laser powder bed fusion deformation, Addit. Manuf. 12 (2016) 108–120.

[10] Y. Cao, X. Lin, N. Kang, L. Ma, L. Wei, M. Zheng, J. Yu, D. Peng, W. Huang, A novel high-efficient finite element analysis method of powder bed fusion additive manufacturing, Addit. Manuf. 46 (2021) 102187.

[11] J.L. Bartlett, X. Li, An overview of residual stresses in metal powder bed fusion, Addit. Manuf. 27 (2019) 131–149.

[12] M. Gouge, E. Denlinger, J. Irwin, C. Li, P. Michaleris, Experimental validation of thermo-mechanical part-scale modeling for laser powder bed fusion processes, Addit. Manuf. 29 (2019) 100771.

[13] X. Liu, X. Liu, G. Kumar, P. Witherell, Scalable path level thermal history simulation of PBF process validated by melt pool images, 2023, arXiv preprint arXiv:2308.02473.

[14] A. Olleak, Z. Xi, Part-scale finite element modeling of the selective laser melting process with layer-wise adaptive remeshing for thermal history and porosity prediction, J. Manuf. Sci. Eng. 142 (12) (2020).

[15] Y. Zhang, V. Shapiro, P. Witherell, A scalable framework for process-aware thermal simulation of additive manufacturing processes, J. Comput. Inf. Sci. Eng. 22 (1) (2022).

[16] M. Pagac, J. Hajnys, R. Halama, T. Aldabash, J. Mesicek, L. Jancar, J. Jansa, Prediction of model distortion by fem in 3D printing via the selective laser melting of stainless steel aisi 316L, Appl. Sci. 11 (4) (2021) 1656.

[17] Y.-C. Wu, C.-H. San, C.-H. Chang, H.-J. Lin, R. Marwan, S. Baba, W.-S. Hwang, Numerical modeling of melt-pool behavior in selective laser melting with random powder distribution and experimental validation, J. Mater Process. Technol. 254 (2018) 72–78.

[18] C. Lüthi, M. Afrasiabi, M. Bambach, An adaptive Smoothed Particle Hydrodynamics (SPH) scheme for efficient melt pool simulations in additive manufacturing, Comput. Math. Appl. 139 (2023) 7–27.

[19] B. Lane, H. Yeung, Process monitoring dataset from the additive manufacturing metrology testbed (AMMT):"Three-dimensional scan strategies", J. Res. Natl. Inst. Stand. Technol. 124 (2019) 1.

[20] B.A. Fisher, B. Lane, H. Yeung, J. Beuth, Toward determining melt pool quality metrics via coaxial monitoring in laser powder bed fusion, Manuf. Lett. 15 (2018) 119–121.

[21] B. Lane, H. Yeung, Process monitoring dataset from the additive manufacturing metrology testbed (AMMT): Overhang part x4, J. Res. Natl. Inst. Stand. Technol. 125 (2020) 1–18.

[22] H. Yeung, B. Lane, A residual heat compensation based scan strategy for powder bed fusion additive manufacturing, Manuf. Lett. 25 (2020) 56–59.

[23] J.G. Michopoulos, A.P. Iliopoulos, J.C. Steuben, A.J. Birnbaum, S.G. Lambrakos, On the multiphysics modeling challenges for metal additive manufacturing processes, Addit. Manuf. 22 (2018) 784–799.

[24] X. Liang, L. Cheng, Q. Chen, Q. Yang, A.C. To, A modified method for estimating inherent strains from detailed process simulation for fast residual distortion prediction of single-walled structures fabricated by directed energy deposition, Addit. Manuf. 23 (2018) 471–486.

[25] M. Bayat, C.G. Klingaa, S. Mohanty, D. De Baere, J. Thorborg, N.S. Tiedje, J.H. Hattel, Part-scale thermo-mechanical modelling of distortions in laser powder bed fusion–analysis of the sequential flash heating method with experimental validation, Addit. Manuf. 36 (2020) 101508.

[26] W. Zhang, M. Tong, N.M. Harrison, Resolution, energy and time dependency on layer scaling in finite element modelling of laser beam powder bed fusion additive manufacturing, Addit. Manuf. 28 (2019) 610–620.

[27] X. Liu, V. Shapiro, Homogenization of material properties in additively manufactured structures, Comput. Aided Des. 78 (2016) 71–82.

[28] M.R. Yavari, K.D. Cole, P. Rao, Thermal modeling in metal additive manufacturing using graph theory, J. Manuf. Sci. Eng. 141 (7) (2019).

[29] R.K. Ganeriwala, N.E. Hodge, J.M. Solberg, Towards improved speed and accuracy of laser powder bed fusion simulations via multiscale spatial representations, Comput. Mater. Sci. 187 (2021) 110112.

[30] J. Liu, G. Li, Q. Sun, H. Li, J. Sun, X. Wang, Understanding the effect of scanning strategies on the microstructure and crystallographic texture of Ti-6Al-4V alloy manufactured by laser powder bed fusion, J. Mater Process. Technol. 299 (2022) 117366.

[31] N. Nadammal, T. Mishurova, T. Fritsch, I. Serrano-Munoz, A. Kromm, C. Haberland, P.D. Portella, G. Bruno, Critical role of scan strategies on the development of microstructure, texture, and residual stresses during laser powder bed fusion additive manufacturing, Addit. Manuf. 38 (2021) 101792.

[32] C. Chen, Z. Xiao, Y. Wang, X. Yang, H. Zhu, Prediction study on in-situ reduction of thermal stress using combined laser beams in laser powder bed fusion, Addit. Manuf. 47 (2021) 102221.

[33] Y. Zhang, V. Shapiro, Linear-time thermal simulation of as-manufactured fused deposition modeling components, J. Manuf. Sci. Eng. 140 (7) (2018).

[34] B. Lane, J. Heigel, R. Ricker, I. Zhirnov, V. Khromschenko, J. Weaver, T. Phan, M. Stoudt, S. Mekhontsev, L. Levine, Measurements of melt pool geometry and cooling rates of individual laser traces on IN625 bare plates, Integr. Mater. Manuf. Innov. 9 (2020) 16–30.

[35] E.R. Denlinger, M. Gouge, J. Irwin, P. Michaleris, Thermomechanical model development and in situ experimental validation of the laser powder-bed fusion process, Addit. Manuf. 16 (2017) 73–80.

[36] N. Schnell, M. Schoeler, G. Witt, S. Kleszczynski, Experimental and numerical thermal analysis of the laser powder bed fusion process using in situ temperature measurements of geometric primitives, Mater. Des. 209 (2021) 109946.

[37] Y. Lu, Z. Yang, J. Kim, H. Cho, H. Yeung, Camera-based coaxial melt pool monitoring data registration for laser powder bed fusion additive manufacturing, in: ASME International Mechanical Engineering Congress and Exposition, vol. 84492, American Society of Mechanical Engineers, 2020, V02BT02A045.

[38] D. Yang, H. Li, S. Liu, C. Song, Y. Yang, S. Shen, J. Lu, Z. Liu, Y. Zhu, In situ capture of spatter signature of SLM process using maximum entropy double threshold image processing method based on genetic algorithm, Opt. Laser Technol. 131 (2020) 106371.

[39] M.T. Andani, R. Dehghani, M.R. Karamooz-Ravari, R. Mirzaeifar, J. Ni, A study on the effect of energy input on spatter particles creation during selective laser melting process, Addit. Manuf. 20 (2018) 33–43.

[40] L.R. Goossens, B. Van Hooreweder, A virtual sensing approach for monitoring melt-pool dimensions using high speed coaxial imaging during laser powder bed fusion of metals, Addit. Manuf. 40 (2021) 101923.

[41] J.A. Mitchell, T.A. Ivanoff, D. Dagel, J.D. Madison, B. Jared, Linking pyrometry to porosity in additively manufactured metals, Addit. Manuf. 31 (2020) 100946.

[42] M.L.G. Grasso, A. Remani, A. Dickins, B.M. Colosimo, R.K. Leach, In-situ measurement and monitoring methods for metal powder bed fusion–An updated review, Meas. Sci. Technol. (2021).

[43] Z. Tan, Q. Fang, H. Li, S. Liu, W. Zhu, D. Yang, Neural network based image segmentation for spatter extraction during laser-based powder bed fusion processing, Opt. Laser Technol. 130 (2020) 106347.

[44] H. Liu, C. Gobert, K. Ferguson, B. Abranovic, H. Chen, J.L. Beuth, A.D. Rollett, L.B. Kara, Inference of highly time-resolved melt pool visual characteristics in laser powder bed fusion from acoustic and thermal emission data, 2023, arXiv preprint arXiv:2310.05289.

[45] M. Rohe, B.N. Stoll, J. Hildebrand, J. Reimann, J.P. Bergmann, Detecting process anomalies in the GMAW process by acoustic sensing with a Convolutional Neural Network (CNN) for classification, J. Manuf. Mater. Process. 5 (4) (2021) 135.

[46] Z. Smoqi, A. Gaikwad, B. Bevans, M.H. Kobir, J. Craig, A. Abul-Haj, A. Peralta, P. Rao, Monitoring and prediction of porosity in laser powder bed fusion using physics-informed meltpool signatures and machine learning, J. Mater Process. Technol. 304 (2022) 117550.

[47] R. Liu, S. Liu, X. Zhang, A physics-informed machine learning model for porosity analysis in laser powder bed fusion additive manufacturing, Int. J. Adv. Manuf. Technol. 113 (7–8) (2021) 1943–1958.

[48] S.A. Shevchik, C. Kenel, C. Leinenbach, K. Wasmer, Acoustic emission for in situ quality monitoring in additive manufacturing using spectral convolutional neural networks, Addit. Manuf. 21 (2018) 598–604.

[49] K. Demir, Z. Zhang, A. Ben-Artzy, P. Hosemann, G.X. Gu, Laser scan strategy descriptor for defect prognosis in metal additive manufacturing using neural networks, J. Manuf. Process. 67 (2021) 628–634.

[50] L. Fang, L. Cheng, J.A. Glerum, J. Bennett, J. Cao, G.J. Wagner, Data-driven analysis of process, structure, and properties of additively manufactured inconel 718 thin walls, npj Comput. Mater. 8 (1) (2022) 126.

[51] K. Jones, Z. Yang, H. Yeung, P. Witherell, Y. Lu, Hybrid modeling of melt pool geometry in additive manufacturing using neural networks, in: International Design Engineering Technical Conferences and Computers and Information in Engineering Conference, vol. 85376, American Society of Mechanical Engineers, 2021, V002T02A031.

[52] Z. Ren, L. Gao, S.J. Clark, K. Fezzaa, P. Shevchenko, A. Choi, W. Everhart, A.D. Rollett, L. Chen, T. Sun, Machine learning–aided real-time detection of keyhole pore generation in laser powder bed fusion, Science 379 (6627) (2023) 89–94.

[53] I.J. Goodfellow, J. Pouget-Abadie, M. Mirza, B. Xu, D. Warde-Farley, S. Ozair, A. Courville, Y. Bengio, Generative adversarial networks, in: Advances in Neural Information Processing Systems, 2014.

[54] P. Isola, J.Y. Zhu, T. Zhou, A.A. Efros, Image-to-image translation with conditional adversarial networks, in: Proceedings - 30th IEEE Conference on Computer Vision and Pattern Recognition, CVPR 2017, vol. 2017-Janua, 2017, pp. 5967–5976, http://dx.doi.org/10.1109/CVPR.2017.632.

[55] H. Chen, X. Liu, Geometry enhanced generative adversarial networks for random heterogeneous material representation, in: International Design Engineering Technical Conferences and Computers and Information in Engineering Conference, vol. 85383, American Society of Mechanical Engineers, 2021, V03AT03A020.

[56] J. Trapp, A.M. Rubenchik, G. Guss, M.J. Matthews, In situ absorptivity measurements of metallic powders during laser powder-bed fusion additive manufacturing, Appl. Mater. Today 9 (2017) 341–349.

[57] M. Matthews, J. Trapp, G. Guss, A. Rubenchik, Direct measurements of laser absorptivity during metal melt pool formation associated with powder bed fusion additive manufacturing processes, J. Laser Appl. 30 (3) (2018) 032302.
[58] P. Isola, J.-Y. Zhu, T. Zhou, A.A. Efros, Image-to-image translation with conditional adversarial networks, in: Proceedings of the IEEE Conference on Computer Vision and Pattern Recognition, 2017, pp. 1125–1134.
[59] pix2pix: Image-to-image translation with a conditional GAN | TensorFlow core — tensorflow.org, 2024, https://www.tensorflow.org/tutorials/generative/pix2pix. (Accessed 18 February 2024).
[60] Y.M. Arısoy, L.E. Criales, T. Özel, Modeling and simulation of thermal field and solidification in laser powder bed fusion of nickel alloy IN625, Opt. Laser Technol. 109 (2019) 278–292.
[61] S. Van der Walt, J.L. Schönberger, J. Nunez-Iglesias, F. Boulogne, J.D. Warner, N. Yager, E. Gouillart, T. Yu, Scikit-image: Image processing in Python, PeerJ 2 (2014) e453.
[62] Y. Zhang, A Scalable Framework for Contact-Aware Thermal Simulation of Additive Manufacturing Processes, The University of Wisconsin-Madison, 2020.
[63] Y. Zhang, V. Shapiro, P. Witherell, Towards thermal simulation of powder bed fusion on path level, in: International Design Engineering Technical Conferences and Computers and Information in Engineering Conference, vol. 59179, American Society of Mechanical Engineers, 2019, V001T02A034.
[64] B. Lane, S. Mekhontsev, S. Grantham, M. Vlasea, J. Whiting, H. Yeung, J. Fox, C. Zarobila, J. Neira, M. McGlauflin, et al., Design, developments, and results from the NIST Additive Manufacturing Metrology Testbed (AMMT), in: 2016 International Solid Freeform Fabrication Symposium, University of Texas at Austin, 2016.